Accuracy versus predictive power in nuclear mass tabulations

Weihu Ye and Yibin Qian*
Department of Applied Physics and MIIT Key Laboratory of Semiconductor Microstructure and Quantum Sensing, Nanjing University of Science and Technology, Nanjing 210094, China

Zhongzhou Ren†
School of Physics Science and Engineering, Tongji University, Shanghai 200092, China

(Received 27 January 2022; accepted 4 August 2022; published 17 August 2022)

The nuclear mass evaluations have been brought into quite an accurate level with the advent of machine learning, while their extrapolations are in great debate as manifested by the large discrepancies between themselves. Here, we present a possible way to heal these existing differences and raise the predictive ability of mass formulas through performing the multi-objective optimization aimed at both the binding energy and the α decay energy. As exemplified by the microscopically inspired Dulfo-Zuker model, the Pareto optimal solutions are found to guarantee the robust mass predictions especially towards the extreme neutron-rich nuclei plus the coherent statistical analysis. Besides effectively avoiding the overfitting problem, our results shed new light on narrowing the window of symmetry energy in nuclear mass formulas serving not only the reliable nuclear dripline but also the stringent equation of state in asymmetric nuclear matter.

DOI: 10.1103/PhysRevC.106.024318

I. INTRODUCTION

Nuclear mass or binding energy has always been one of the most central issues in nuclear physics, due to its direct connection with the fundamental nucleon-nucleon interaction [1]. The first successful mass formula, namely the liquid drop (LD) model, had not only verified the understanding of nuclear force at that time but also intrigued the nuclear fission research and the application of nuclear energy [2]. Nowadays, the tiny nucleus is correlated with the infinite nuclear matter via the symmetry energy, further simulating the broad physical interest on the nuclear binding energy [3]. On the other hand, the mass of neutron-rich nuclei is a key factor determining the *r*-process path of the nucleosynthesis, which serves the full knowledge of the formation and evolution of elements heavier than iron in the universe [4–6]. Nonetheless, although the recent decades were a fertile breeding ground for precisely measuring nuclear mass with the advent of high-performance facilities of radioactive ion beams, for the foreseeable future, it is still impossible to experimentally explore the very short-lived nuclei towards the neutron dripline [7,8]. The nuclear mass formulas are therefore in great demand especially concerning the reliable extrapolation besides the high accuracy.

Among the current market of mass models, the popular macroscopic-microscopic (mac-mic) approach [9–11] consists of the (modified) LD part and the microscopic shell plus pairing corrections, while the (non)relativistic energy density functionals (EDFs) [12,13] describe the nuclear binding energy in a more microscopic way. Different from these global mass formulas, the local mass relationship or the binding energy (BE) systematics has also been employed to perform mass evaluations in some specific regions [14,15]. With the introduction and development of machine learning strategies like the Bayesian neural network, the accuracies of various BE evaluations, in the measured mass region, have reached a quite high level towards the so-called chaos limit [16–20]. Considering these, it seems that there are few studies one can do about the theoretical nuclear mass framework. However, one question naturally arises: To what extent can we trust these nuclear mass extrapolations? Let us pay attention to two serious issues before answering this. First, there are actually quite large deviations between different BE evaluations based on the aforementioned mass formulas in terms of the model itself [9]. Even in the same Hartree-Fock-Bogoliubov mass formulas, their extrapolations would vary drastically with the update [21,22]. Second, after including machine learning, the binding energy prediction may produce odd values at large extrapolating distance, not to mention the instabilities caused by the large number of parameters in the black box of machine learning. Meanwhile, the extrapolation abilities of these AI approaches are found to be dependent on the employed mass formulas [23]. With these in mind, one may conclude that the extrapolation of nuclear mass formulas should be given more attention rather than the single pursuit of high accuracy in the known region.

In fact, the present mass formulas are still derived from inaccurate models, in which the missing physics would be involved in the parameter-fitting process. The adjusted parameters could, in turn, damage the predictive ability of mass models. In this study, we report the rigid multi-objective

*qyibin@njust.edu.cn
†zren@tongji.edu.cn

optimization (MOO) in the nuclear mass model to tackle this issue. As is well known, the binding energy difference corresponds to other observables, like the decay energy and the nucleon separation energy. Recently, α decay spectra have been paid special attention due to their unique role played in the identification of new superheavy elements [24], the understanding of the shell structure [25,26], and the probe into the α clustering in heavy nuclei [27,28]. Plenty of α decay energy (Q_α) data have therefore accumulated, which can be settled as another independent target for the mass formulas. Moreover, the neutron skin thickness of ^{208}Pb is reported as $\Delta R_{np} = 0.283 \pm 0.071$ fm in the PREX II measurement [29], implying a large slope parameter $L = 106 \pm 37$ MeV in the nuclear equation of state and the symmetry energy coefficient (SEC) $S_0 = 38.1 \pm 4.7$ MeV [30]. These values, larger than most of the theoretical predictions, are in a subtle relationship with the SEC in the mass formulas [31]. It is of physical importance to see what will happen to the symmetry energy term after the mass formulas are further constrained via the MOO procedure.

II. THEORETICAL FRAMEWORK

Multi-objective optimization is a very common situation faced by people in real life, such as engineering and economics [32–34], which aims at the balance between (more than one) objectives. A multi-objective problem can be simplified as follows:

$$\begin{aligned} \min \quad & F(x) = (f_1(x), \ldots, f_m(x)), \\ \text{s.t.} \quad & x \subset \Omega, \\ & lb \leqslant x_i \leqslant ub, \end{aligned} \tag{1}$$

where $f_i(x)$ is the objective function associated with an identical kernel (i.e., the mass formula here), and $x = (x_1, x_2, \ldots, x_m)$ is the decision variables constructing the decision space Ω. Each x_i is restricted between the lower and upper boundaries. The main method of MOO is the evolution algorithm, in which the variable set x is considered as an individual in one generation during the population-evolution-like process. The essence is that one individual t will be replaced by another s if $f_i(s) \leqslant f_i(t)$ for all $i = 1, 2, \ldots, m$ and $f_i(s) < f_i(t)$ for at least one objective. To present more details, a two-objective problem plus two variables is illustrated in Fig. 1, where the decision space Ω at the left panel corresponds to the objective space at the right panel. As shown in the latter space, the individual (or the variable set) A is actually the optimal point for the target $f_1(x)$, while the individual D corresponds to the function $f_2(x)$. The boundary line from A to D, as denoted by the dashed line, represents all the possible variable sets, namely the so-called Pareto front (PF) solution. The multi-objective evolution algorithm (MOEA) is exactly implemented to find as many as possible PF solutions. As one of the most frequently used MOEAs, the non-dominated sorting genetic algorithm-II (NSGA-II), is adopted here due to its relatively-low computing and storage complexities in second generation algorithms [35]. The main procedure of the NSGA-II is listed below:

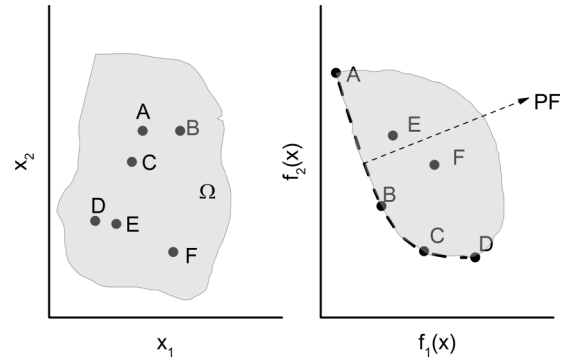

FIG. 1. A sketch for the two-objective optimization problem in the case of two variables. The variables x_1, x_2 construct the decision space in the left panel, corresponding to the objective space of $f_1(x)$ and $f_2(x)$. These points A, B, C, ... present the individuals generated in each population of the evolution algorithm, and the symbol "PF" is abbreviated from the Pareto front solution.

(1) Population initialization: Set generation of population $t = 0$ at initial time. Create a parent population P_t with N individuals randomly, corresponding to parameter sets of the mass formula here.
(2) Population evolution: Perform selection, crossover, mutation on population P_t, and obtain offspring population Q_t with equal members. Combine P_t and Q_t together to yield a $2N$ population R_t.
(3) Based on the computed objective values plus a non-dominated sorting process, each individual in R_t is assigned with a Pareto rank. All the individuals are then classified into different groups, namely $\{O_i\}$ as shown in panel (a) of Fig. 2, via their rank values.
(4) The population P_{t+1} is set as $\emptyset$. The individuals from O_1 to O_j ($j \geqslant 1$) are added into P_{t+1} in order until

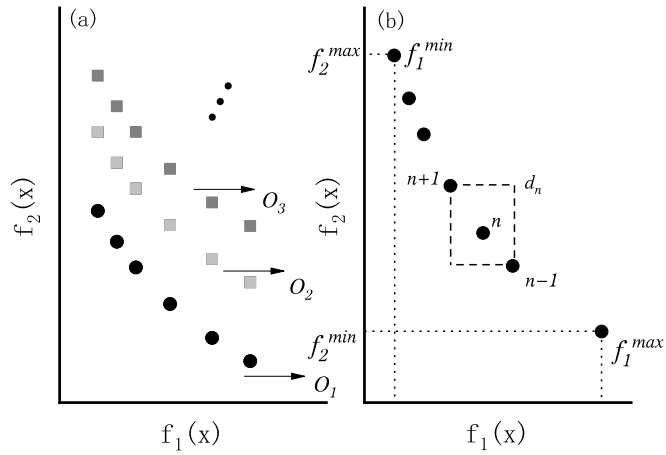

FIG. 2. On the left panel, the Pareto rank of each individual is obtained by using non-dominated sorting procedure [35–37], i.e., the individuals are divided into finite sets with the different priority, namely, $O_1, O_2, O_3, \ldots$. The crowding distance is graphically illustrated at the right panel, where the $f_{1,2}^{\max}$ and $f_{1,2}^{\min}$ are the maximum and minimum values for the objective function $f_{1,2}$, respectively. The d_n represents the crowding distance for individual n.

$\sum_{i=1}^{k} O_i \leqslant N$, $\sum_{i=1}^{k+1} O_i > N$. At this moment, the individuals of O_{k+1} will be partially taken into P_{t+1}.

(5) The prior members in O_{k+1} are chosen to fulfill the P_{t+1} with the size of N via a crowding distance sorting method. During this, as shown in panel (b) of Fig. 2, the crowding distance is calculated by $d_n = \frac{f_1[n-1]-f_1[n+1]}{f_1^{\max}-f_1^{\min}} + \frac{f_2[n-1]-f_2[n+1]}{f_2^{\max}-f_2^{\min}}$.

(6) If the fixed number of iterations is reached or the evolutive results are convergent, the program returns the Pareto front and ends. If not, the algorithm continues and jumps to step 2.

During the above procedure, each individual is attached with two signs, namely the Pareto rank and the crowding distance d. In practice, the crowded-comparison operator ($\prec_n$) is defined in the NSGA-II algorithm to determine which solution is better. The individual A is better than B ($A \prec_n B$) if $\text{rank}(A) \leqslant \text{rank}(B)$ and $d_A > d_B$, which is the specific implementation of the PF solution in the MOO scheme. In addition, there are two prominent attributes for the NSGA-II method. One is the fast non-dominated sorting approach to speed up the convergence, and the other is the crowding-distance computation to ensure a uniform distribution of solutions and a diversity of individuals (see more details in Refs. [35–42] and references therein).

When it comes to the present study, the two objectives are, respectively, the root-mean-square deviation (RMSD) between theory and experiment for the nuclear binding energy and the α decay energy based on the mass formulas, namely $f_1 = \sigma_{\rm BE}$ and $f_2 = \sigma_{Q_\alpha}$. The latter quantity is derived from the mass difference, i.e., $Q_\alpha = \text{BE}(Z-2, N-2) + \text{BE}_\alpha - \text{BE}(Z, N)$. The focus point then comes to the kernel mass formulas for the nuclear BE computation. Given the massive samplings and computation costs, the classical DZ10 mass formula is employed to proceed the MOEA analysis due to its microscopic foundation. Another benefit is that one can readily check out the symmetry energy coefficient in this mass formula, which is written as

$$\text{BE}_{DZ10} = a_1 V_C + a_2(M+S) - a_3\frac{M}{\rho} + a_4 V_P - a_5 V_T + a_6 V_{TS} + a_7 s_3 - a_8\frac{s_3}{\rho} + a_9 s_4 + a_{10} d_4, \quad (2)$$

where the coefficient $\{a_i\}$ means the variable set x to be determined via the NSGA-II strategy. These capital terms, in the above formula, are actually mapped from the macroscopic liquid drop model, whereas the residual terms present the microscopic corrections within the shell-model context (see Refs. [43,44]).

III. RESULTS AND DISCUSSIONS

By fitting the available experimental data of BE and Q_α from [45] AME20 (with the error bar below 100 keV), the PF solution line is shown for the DZ10 mass formula in Fig. 3. One may note that the varying range of σ_{Q_α} is only about 0.05 MeV, whereas the α decay half-life is very sensitive to the Q_α value. The change of 0.05 MeV in decay energy can produce a 50 percent adaption in decay half-life. On the other hand, the range of $\sigma_{\rm BE}$, from the left boundary to the converging point, is not large either. Interestingly, there are a large number of possible parameter choices even in such a small range of σ_{Q_α} and $\sigma_{\rm BE}$, which naturally supplies the statistical analysis on the model uncertainty. Based on these PF results, our attention is then paid to two consequent influences, namely the new dripline of the nuclear chart plus the extrapolation to the neutron rich side and the interesting symmetry energy coefficients. Before that, let us concern ourselves with a simple question: Why do we not combine the two objectives into a single one? Indeed, this is a simple way to solve the multi-objective optimization, while the combination method is a serious problem. For example, one cannot decide if addition or multiplication is better for combining two objectives. Yet, the fitting result, by minimizing the total value of $\sigma_{\rm BE}$ and σ_{Q_α}, is also listed in the last column of Table I for comparison. In this table, the first column presents the present solutions via the MOO procedure. Meanwhile, the single objective optimization of binding energy, namely the top point in Fig. 3, is listed

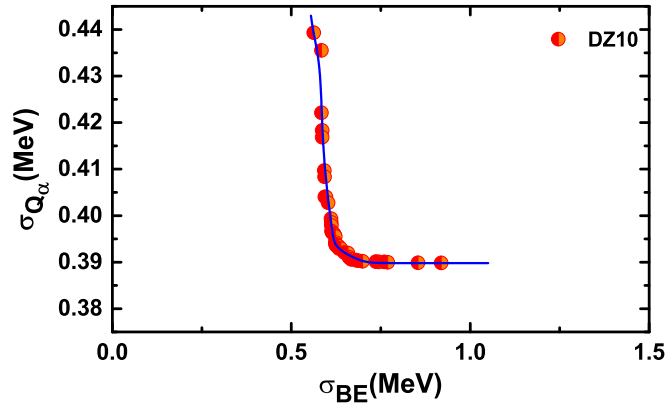

FIG. 3. The objective space governed by the $\sigma_{\rm BE}$ (horizontal) and σ_{Q_α} (vertical) values for the DZ10 mass formula. Note that each marker point presents a PF solution guided by the blue line. The BE data with $N, Z \geqslant 8$, and Q_α values with $A \geqslant 105$ are taken from the AME20 [45].

TABLE I. The resultant parameters from the Pareto front solutions for the DZ10 formula. Case I indicates the single optimization of binding energy, while Case II comes from minimizing the value of $\sigma_{\rm BE} + \sigma_{Q_\alpha}$.

Quantity	Present	Case I	Case II
a_1	0.705 ± 0.001	0.705	0.704
a_2	17.735 ± 0.03	17.747	17.734
a_3	16.207 ± 0.093	16.251	16.206
a_4	5.906 ± 0.58	6.102	6.09
a_5	37.303 ± 0.097	37.356	37.253
a_6	52.757 ± 0.568	52.661	52.282
a_7	0.438 ± 0.009	0.463	0.427
a_8	2.006 ± 0.041	2.104	1.932
a_9	0.022 ± 0.0005	0.021	0.022
a_{10}	39.602 ± 0.591	41.48	40.731
σ_{Q_α}	0.397 ± 0.011	0.439	0.401
σ_{BE}	0.66 ± 0.083	0.562	0.577

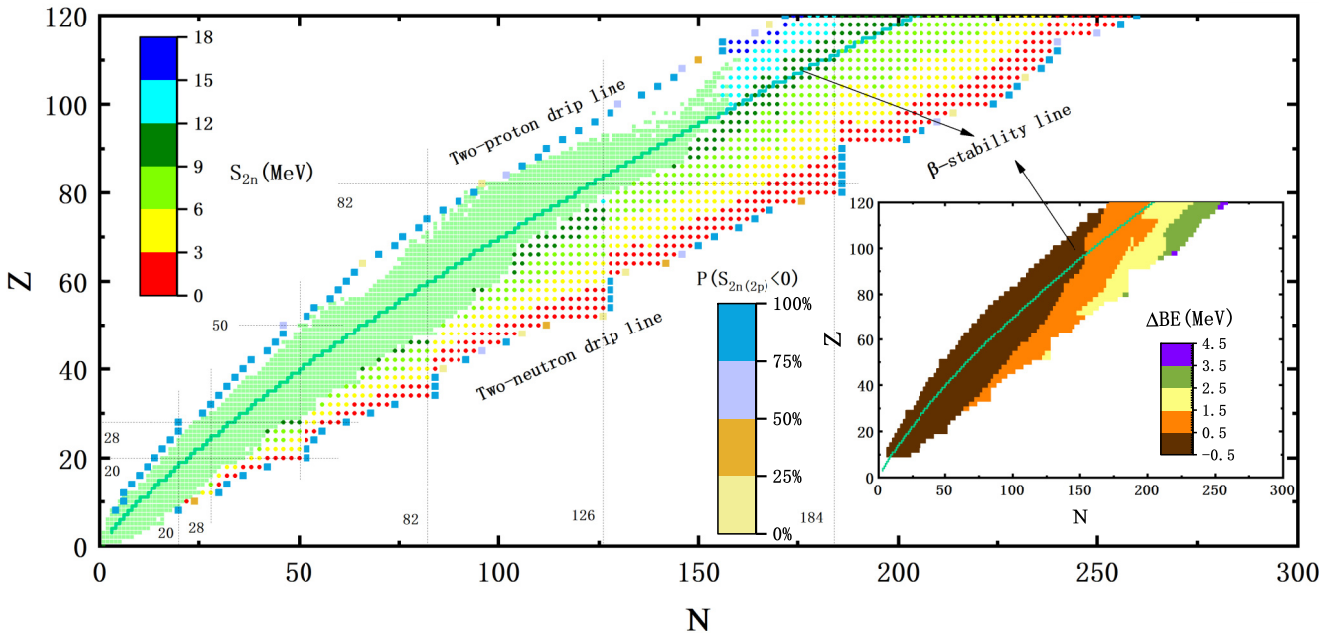

FIG. 4. The nuclear chart of even-even nuclei generated by the MOO-constrained DZ10 formulas with possible PF solutions, including the β-stability line to guide the eye. The available nuclides, according to the AME20 compilation [45], are denoted by the green squares, and the S_{2n} values of unknown neutron-rich nuclei are listed in colorful circles as well. Note that the S_{2n} value of one nucleus is obtained by averaging all the results from the DZ10 evaluation with PF solutions. For each isotopic chain, the first nuclei above the proton and neutron dripline nuclei are both denoted with colorful squares. The "P" symbol corresponds to the percentage of PF solutions resulting in the negative two-nucleon separation energies. The window in the lower right corner presents a typical example of mass differences (see details in text).

in the second column. It is found that the balance between the present objectives can be achieved with the MOO strategy in contrast to the single-objective Case I, while the simple treatment of two-objective problem, i.e., Case II, is already included in the present approach.

Based on the microscopic DZ10 model, the first MOO-constrained chart of even-even nuclides is demonstrated in Fig. 4. The chart boundary is regulated by the two-neutron and two-proton drip lines, which are determined by the two nucleon separation energies (S_{2p} and S_{2n}) from the BE extrapolation of DZ10 formula within the present MOO strategy. Similar dripline nuclei are engendered by the dozens of PF parameter sets, while the first nuclei with $S_{2n(2p)} < 0$ of one isotopic chain are presented with the percentage of all the PF solutions yielding the negative separation energies. There are some uncertainties for these nonexistent nuclei between the major shell closures. The experimentally known nuclei are found to be all located in the present nuclear chart. Meanwhile, the two-proton dripline is nearly touched by the experiment, in particular around the $N = 100$ region, which deserves further attention according to the present results. As compared, there are plenty of blanks below the β-stability line towards the extreme neutron-rich side, supplying the full knowledge of the astrophysical r process. Of course, the direct input, for the simulation of the element evolution in the universe, is not only the nucleon separation energy but also the mass value. Despite the small discrepancies of the S_{2p} or S_{2n} values, there are actually nontrivial deviations for the BE extrapolations in the neutron-rich region from different PF solutions of the DZ10 mass formula. There is a representative example in the lower right corner of Fig. 4. The mass difference ΔBE is derived from the two best DZ10 mass evaluations for the target of $\sigma_{\rm BE}$, corresponding to the two top points in Fig. 3. Clearly, the ΔBE value becomes increasingly large when it comes to the unknown region. Considering the tiny distance between these two points in the figure, one can conjecture that the mass evaluation must be very careful and it is a normal event for the large differences between results from various mass formulas. Fortunately, if one arbitrarily chooses two parameter sets in the middle of the PF solution line, the eventual binding energies are closer with each other even in the very neutron-rich region, as displayed in Fig. 5.

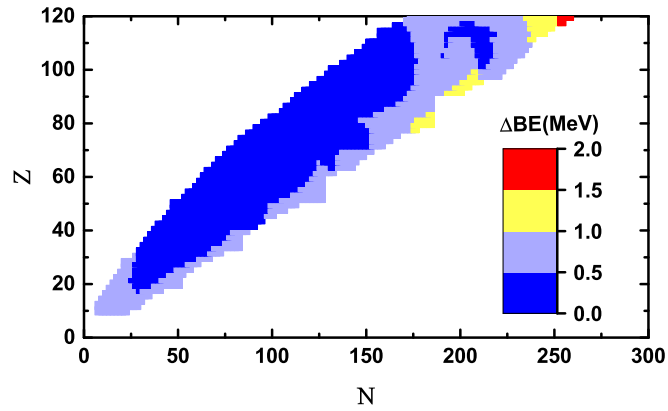

FIG. 5. The differences between two DZ10 mass evaluations from the solutions in the middle of the PF line shown in Fig. 3.

Here, the ΔBE value is reduced by about 50–60 percent as compared to the case of two optimal solutions for the single BE fitting. Through these comparisons, one may conclude that the MOO-constrained mass tabulation, correcting the possible overfitting problem, is more reasonable in terms of the model uncertainty.

Last but not least, let us pay special attention to the symmetry energy term in mass formulas of finite nuclei, which is supposed to be related with the symmetry energy in the asymmetric nuclear matter. The symmetry energy in mass formulas is commonly written by $a_{sym}(A)(N-Z)^2/A$, where the coefficient is here adopted as $a_{sym}(A) = a_5 - a_6 A^{-1/3}$ [46]. The energy per nucleon of the asymmetric nuclear matter, defining the equation of state (EOS), is $e(\rho,\delta) = e(\rho,0) + S(\rho)\delta^2 + O(\delta^4)$ with isospin asymmetry $\delta = (\rho_n - \rho_p)/\rho$ plus the nucleon density $\rho = \rho_n + \rho_p$. If neglecting the higher order terms in the EOS, the most significant challenge comes from the large uncertainty of the symmetry energy coefficient (SEC) $S(\rho)$. Extensive efforts have been devoted to unravelling the symmetry energy coefficient of EOS or its slope and curvature parameters [31,47,48]. Among several proposals on S_ρ [49,50], one specific formula delivered from the transport method [51],

$$S(\rho) = S(\rho_0)\left(\frac{\rho}{\rho_0}\right)^{\gamma}, \tag{3}$$

is used here to proceed the following analysis. There exists a generic equation between the SEC of nuclear EOS and that in the mass formula, namely $S(\rho_A) = a_{sym}(A)$. One can then easily put forward the asymptotic situation $a_{sym}(A \to \infty) = S(\rho_0)$. Another condition can be from $a_{sym}(A = 208) = S(\rho_{208})$ of ^{208}Pb, whose density ρ_{208} is fixed at 0.1 fm^{-3} [52]. In this way, the specific $S(\rho)$ is obtained, resulting in the slope parameter via $L = 3\rho\frac{\partial S(\rho)}{\partial \rho}|_{\rho_0}$. Given the high linear relationship between the slope parameter and the neutron skin thickness of nuclei [53], one can also evaluate the Δ_{np}^{208} value. Figure 6 presents the distribution of the slope parameter and the neutron skin thickness of ^{208}Pb deduced from the present PF solutions via the above procedure. In general, these two quantities are consistent with the popular theoretical predictions, while a thinner neutron skin is obtained for ^{208}Pb in contrast with the PREX-II experiment [29].

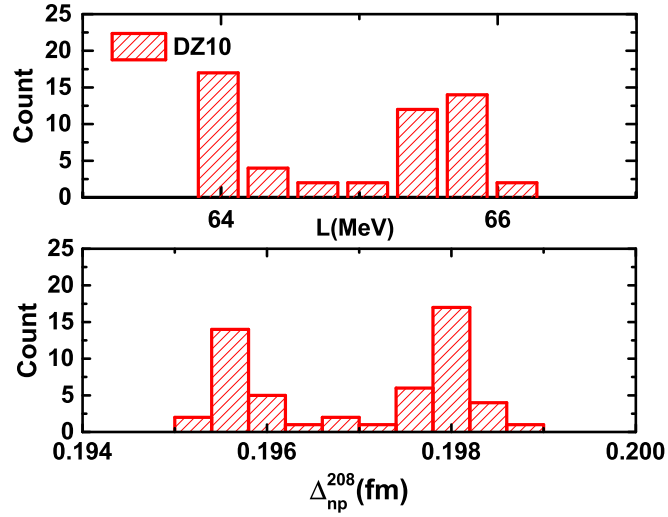

FIG. 6. Histograms of the slope parameter L and the neutron skin thickness of ^{208}Pb by using the symmetry energy coefficient of the DZ0 mass formula after the multi-objective optimization.

IV. SUMMARY

In summary, the urgently requested mass extrapolation is still unsatisfied especially towards the neutron dripline of the nuclear chart. We report a first multi-objective optimization (MOO) on the nuclear mass formula to further constrain the model itself rather than the single pursuit of high accuracy in the known region. By matching the experimental data of both the binding energy and the α decay energy, the parametrization of the DZ10 mass formula is refreshed as the PF solutions plus the statistical analysis. With the parameter sets in the middle of the PF line, the differences of mass evaluations indeed tend to decrease to a great extent, guaranteeing the reliability at the level of the mass formula itself. Encouraged by this, new limits are proposed for the microscopic DZ10 mass tables, serving more reasonable suggestions for the experimental design. The slope parameter in the nuclear EOS is then determined in the range of 63.8–66.2 MeV through the MOO-constrained SEC of mass formulas, while the neutron skin thickness of ^{208}Pb is extracted to be thinner than the recent extraction from the electron scattering experiment. It is expected to check the extension of the MOO strategy to not only other global mass tables but also nuclear structural studies such as the single particle resonance.

ACKNOWLEDGMENTS

This work is supported by the National Natural Science Foundation of China (Grants No. 12075121, No. 11605089, No. 12035011, No. 11975167, No. 11535004, and No. 11761161001), and by the Natural Science Foundation of Jiangsu Province (Grants No. BK20190067 and No. BK20150762), and by the National Major State Basic Research and Development Program of China (Grant No. 2016YFE0129300).

[1] D. Lunney, J. Pearson, and C. Thibault, Rev. Mod. Phys. **75**, 1021 (2003).
[2] P. Möller and A. Sierk, Int. J. Mass Spectrom. **349–350**, 19 (2013).
[3] C. Horowitz, E. Brown, Y. Kim, W. Lynch, R. Michaels, A. Ono, J. Piekarewicz, M. Tsang, and H. Wolter, J. Phys. G: Nucl. Part. Phys. **41**, 093001 (2014).
[4] A. C. Larsen, A. Spyrou, S. N. Liddick, and M. Guttormsen, Prog. Part. Nucl. Phys. **107**, 69 (2019).
[5] T. Yamaguchi, H. Koura, Y. A. Litvinov, and M. Wang, Prog. Part. Nucl. Phys. **120**, 103882 (2021).

[6] J. Erler, N. Birge, M. Kortelainen, W. Nazarewicz, E. Olsen, A. M. Perhac, and M. Stoitsov, Nature (London) **486**, 509 (2012).

[7] M. Mumpower, R. Surman, G. McLaughlin, and A. Aprahamian, Prog. Part. Nucl. Phys. **87**, 116 (2016).

[8] R. Utama, J. Piekarewicz, and H. B. Prosper, Phys. Rev. C **93**, 014311 (2016).

[9] M. Liu, N. Wang, Y. Deng, and X. Wu, Phys. Rev. C **84**, 014333 (2011).

[10] P. Möller, W. D. Myers, H. Sagawa, and S. Yoshida, Phys. Rev. Lett. **108**, 052501 (2012).

[11] G. Royer, M. Guilbaud, and A. Onillon, Nucl. Phys. A **847**, 24 (2010).

[12] M. Kortelainen, J. McDonnell, W. Nazarewicz, E. Olsen, P.-G. Reinhard, J. Sarich, N. Schunck, S. M. Wild, D. Davesne, J. Erler, and A. Pastore, Phys. Rev. C **89**, 054314 (2014).

[13] A. V. Afanasjev and S. E. Agbemava, Phys. Rev. C **93**, 054310 (2016).

[14] J. Barea, A. Frank, J. G. Hirsch, P. Van Isacker, S. Pittel, and V. Velázquez, Phys. Rev. C **77**, 041304(R) (2008).

[15] G. Garvey, W. Gerace, R. Jaffe, I. Talmi, and I. Kelson, Rev. Mod. Phys. **41**, S1 (1969).

[16] Z. Niu and H. Liang, Phys. Lett. B **778**, 48 (2018).

[17] R. Utama and J. Piekarewicz, Phys. Rev. C **96**, 044308 (2017).

[18] A. Pastore, D. Neill, H. Powell, K. Medler, and C. Barton, Phys. Rev. C **101**, 035804 (2020).

[19] Z. Niu, H. Liang, B. Sun, Y. Niu, J. Guo, and J. Meng, Sci. Bull. **63**, 759 (2018).

[20] L. Neufcourt, Y. Cao, S. A. Giuliani, W. Nazarewicz, E. Olsen, and O. B. Tarasov, Phys. Rev. C **101**, 044307 (2020).

[21] S. Goriely, N. Chamel, and J. M. Pearson, Phys. Rev. C **82**, 035804 (2010).

[22] S. Goriely, N. Chamel, and J. M. Pearson, Phys. Rev. C **88**, 024308 (2013).

[23] Z. M. Niu, J. Y. Fang, and Y. F. Niu, Phys. Rev. C **100**, 054311 (2019).

[24] Y. T. Oganessian and V. Utyonkov, Rep. Prog. Phys. **78**, 036301 (2015).

[25] A. N. Andreyev, M. Huyse, P. Van Duppen, C. Qi, R. J. Liotta, S. Antalic, D. Ackermann, S. Franchoo, F. P. Heßberger, S. Hofmann, I. Kojouharov, B. Kindler, P. Kuusiniemi, S. R. Lesher, B. Lommel, R. Mann, K. Nishio, R. D. Page, B. Streicher, Š. Šáro, B. Sulignano, D. Wiseman, and R. A. Wyss, Phys. Rev. Lett. **110**, 242502 (2013).

[26] L. Ma, Z. Y. Zhang, Z. G. Gan, X. H. Zhou, H. B. Yang, M. H. Huang, C. L. Yang, M. M. Zhang, Y. L. Tian, Y. S. Wang, H. B. Zhou, X. T. He, Y. C. Mao, W. Hua, L. M. Duan, W. X. Huang, Z. Liu, X. X. Xu, Z. Z. Ren, S. G. Zhou, and H. S. Xu, Phys. Rev. Lett. **125**, 032502 (2020).

[27] Z. Y. Zhang, H. B. Yang, M. H. Huang, Z. G. Gan, C. X. Yuan, C. Qi, A. N. Andreyev, M. L. Liu, L. Ma, M. M. Zhang, Y. L. Tian, Y. S. Wang, J. G. Wang, C. L. Yang, G. S. Li, Y. H. Qiang, W. Q. Yang, R. F. Chen, H. B. Zhang, Z. W. Lu, X. X. Xu, L. M. Duan, H. R. Yang, W. X. Huang, Z. Liu, X. H. Zhou, Y. H. Zhang, H. S. Xu, N. Wang, H. B. Zhou, X. J. Wen, S. Huang, W. Hua, L. Zhu, X. Wang, Y. C. Mao, X. T. He, S. Y. Wang, W. Z. Xu, H. W. Li, Z. Z. Ren, and S. G. Zhou, Phys. Rev. Lett. **126**, 152502 (2021).

[28] J. Tanaka, Z. Yang, S. Typel, S. Adachi, S. Bai, P. van Beek, D. Beaumel, Y. Fujikawa, J. Han, S. Heil *et al.*, Science **371**, 260 (2021).

[29] D. Adhikari, H. Albataineh, D. Androic, K. Aniol, D. Armstrong, T. Averett, C. A. Gayoso, S. Barcus, V. Bellini, R. Beminiwattha *et al.*, Phys. Rev. Lett. **126**, 172502 (2021).

[30] B. T. Reed, F. J. Fattoyev, C. J. Horowitz, and J. Piekarewicz, Phys. Rev. Lett. **126**, 172503 (2021).

[31] R. Essick, P. Landry, A. Schwenk, and I. Tews, Phys. Rev. C **104**, 065804 (2021).

[32] R. T. Marler and J. S. Arora, Struct. Multidiscip. Optim. **26**, 369 (2004).

[33] P. Ngatchou, A. Zarei, and A. El-Sharkawi, *Proceedings of the 13th International Conference on Intelligent Systems Application to Power Systems* (IEEE, Arlington, VA, USA, 2005), pp. 84–91

[34] M. G. C. Tapia and C. A. C. Coello, *2007 IEEE Congress on Evolutionary Computation* (IEEE, Singapore, 2007), pp. 532–539.

[35] F.-A. Fortin and M. Parizeau, *Proceedings of the 15th Annual Conference on Genetic and Evolutionary Computation* (Association for Computing Machinery, Amsterdam, The Netherlands, 2013), pp. 623–630.

[36] K. Deb, A. Pratap, S. Agarwal, and T. Meyarivan, IEEE Trans. Evol. Comput. **6**, 182 (2002).

[37] Jazzbin *et al.*, GEATPY: The genetic and evolutionary algorithm toolbox with high performance in PYTHON, 2020.

[38] K. Deb, S. Agrawal, A. Pratap, and T. Meyarivan, *International Conference on Parallel Problem Solving from Nature* (Springer, Berlin, 2000), pp. 849–858.

[39] H. Li and Q. Zhang, IEEE Trans. Evol. Comput. **13**, 284 (2008).

[40] T. M. Hamdani, J.-M. Won, A. M. Alimi, and F. Karray, *International Conference on Adaptive and Natural Computing Algorithms* (Springer, Berlin, 2007), pp. 240–247.

[41] S. Verma, M. Pant, and V. Snasel, IEEE Access **9**, 57757 (2021).

[42] M. Köppen and K. Yoshida, *International Conference on Evolutionary Multi-Criterion Optimization* (Springer, Berlin, 2007), pp. 727–741.

[43] J. Duflo and A. P. Zuker, Phys. Rev. C **52**, R23 (1995).

[44] J. Mendoza-Temis, J. G. Hirsch, and A. P. Zuker, Nucl. Phys. A **843**, 14 (2010).

[45] M. Wang, W. Huang, F. Kondev, G. Audi, and S. Naimi, Chin. Phys. C **45**, 030003 (2021).

[46] M. Centelles, X. Roca-Maza, X. Vinas, and M. Warda, Phys. Rev. Lett. **102**, 122502 (2009).

[47] Z. W. Liu, Z. Qian, R. Y. Xing, J. R. Niu, B. Y. Sun *et al.*, Phys. Rev. C **97**, 025801 (2018).

[48] J. Estee, W. Lynch, C. Tsang, J. Barney, G. Jhang, M. Tsang, R. Wang, M. Kaneko, J. Lee, T. Isobe *et al.*, Phys. Rev. Lett. **126**, 162701 (2021).

[49] M. Di Toro, V. Baran, M. Colonna, and V. Greco, J. Phys. G: Nucl. Part. Phys. **37**, 083101 (2010).

[50] Y. Wang, Q. Li, Y. Leifels, and A. Le Fèvre, Phys. Lett. B **802**, 135249 (2020).

[51] L.-W. Chen, C. M. Ko, and B.-A. Li, Phys. Rev. Lett. **94**, 032701 (2005).

[52] J. Dong, W. Zuo, J. Gu, and U. Lombardo, Phys. Rev. C **85**, 034308 (2012).

[53] X. Roca-Maza, M. Centelles, X. Viñas, and M. Warda, Phys. Rev. Lett. **106**, 252501 (2011).